AFRL-RQ-WP-TR-2016-0118

COMPARISON OF FEMTOSECOND- AND NANOSECOND-TWO-PHOTON-ABSORPTION LASER-INDUCED FLUORESCENCE (TALIF) OF ATOMIC OXYGEN IN ATMOSPHERIC PRESSURE PLASMAS

James D. Scofield (AFRL/RQQE) and James R. Gord (AFRL/RQTC)

Electrical Systems Branch, Power and Control Division (AFRL/RQQE)
Combustion Branch, Turbine Engine Division (AFRL/RQTC)

Jacob B. Schmidt and Sukesh Roy

Spectral Energies LLC

Brian Sands

UES, Inc.

AUGUST 2016
Final Report

AIR FORCE RESEARCH LABORATORY
AEROSPACE SYSTEMS DIRECTORATE
WRIGHT-PATTERSON AIR FORCE BASE, OH 45433-7541
AIR FORCE MATERIEL COMMAND
UNITED STATES AIR FORCE

NOTICE AND SIGNATURE PAGE

This report was cleared for public release by the USAF 88th Air Base Wing (88 ABW) Public Affairs Office (PAO) and is available to the general public, including foreign nationals.

Copies may be obtained from the Defense Technical Information Center (DTIC) (http://www.dtic.mil).

AFRL-RQ-WP-TR-2016-0118 HAS BEEN REVIEWED AND IS APPROVED FOR PUBLICATION IN ACCORDANCE WITH ASSIGNED DISTRIBUTION STATEMENT.

*//Signature//

JAMES D. SCOFIELD
Program Manager
Electrical Systems Branch
Power and Control Division

//Signature//

GREGORY L. FRONISTA, Chief
Electrical Systems Branch
Power and Control Division
Aerospace Systems Directorate

//Signature//

BRYAN J. CANNON, Principal Scientist
Power and Control Division
Aerospace Systems Directorate

REPORT DOCUMENTATION PAGE

1. REPORT DATE *(DD-MM-YY)*	2. REPORT TYPE	3. DATES COVERED *(From - To)*
August 2016	Final	29 November 2012 – 22 August 2016

4. TITLE AND SUBTITLE
COMPARISON OF FEMTOSECOND- AND NANOSECOND-TWO-PHOTON-ABSORPTION LASER-INDUCED FLUORESCENCE (TALIF) OF ATOMIC OXYGEN IN ATMOSPHERIC PRESSURE PLASMAS

5a. CONTRACT NUMBER
In-house

5b. GRANT NUMBER

5c. PROGRAM ELEMENT NUMBER
61102F

6. AUTHOR(S)
James D. Scofield (AFRL/RQQE)
James R. Gord (AFRL/RQTC)
Jacob B. Schmidt and Sukesh Roy (Spectral Energies LLC)
Brian Sands (UES, Inc.)

5d. PROJECT NUMBER
3001

5e. TASK NUMBER

5f. WORK UNIT NUMBER
Q12A

7. PERFORMING ORGANIZATION NAME(S) AND ADDRESS(ES)

Electrical Systems Branch, Power and Control Division (AFRL/RQQE)
Combustion Branch, Turbine Engine Division (AFRL/RQTC)
Air Force Research Laboratory, Aerospace Systems Directorate
Wright-Patterson Air Force Base, OH 45433-7541
Air Force Materiel Command, United States Air Force

Spectral Energies LLC
Dayton, OH 45431

UES, Inc.
Dayton, OH 45432

8. PERFORMING ORGANIZATION REPORT NUMBER
AFRL-RQ-WP-TR-2016-0118

9. SPONSORING/MONITORING AGENCY NAME(S) AND ADDRESS(ES)
Air Force Research Laboratory
Aerospace Systems Directorate
Wright-Patterson Air Force Base, OH 45433-7541
Air Force Materiel Command
United States Air Force

10. SPONSORING/MONITORING AGENCY ACRONYM(S)
AFRL/RQQE

11. SPONSORING/MONITORING AGENCY REPORT NUMBER(S)
AFRL-RQ-WP-TR-2016-0118

12. DISTRIBUTION/AVAILABILITY STATEMENT
Approved for public release. Distribution is unlimited.

13. SUPPLEMENTARY NOTES
PA Case Number: 88ABW-2016-3299; Clearance Date: 30 June 2016.
This is a work of the U.S. Government and is not subject to copyright protection in the United States.

14. ABSTRACT
Absolute number densities of atomic species produced by nanosecond duration, repetitively pulsed electric discharges are measured by two-photon absorption laser-induced fluorescence (TALIF). Unique to this work is the development of femtosecond-laser-based TALIF (fs-TALIF). Fs-TALIF offers a number of advantages compared to more conventional ns-pulse-duration laser systems, including better accuracy of direct quenching measurements in highly collisional environments, significantly reduced photolytic interference including photo-dissociation and photo-ionization, higher signal and increased laser-pulse bandwidth, the ability to collect two-dimensional images of atomic species number densities with high spatial resolution, and much higher laser repetition rates allowing for more efficient and accurate measurements of atomic species number densities. In order to fully quantify these advantages, atomic oxygen TALIF signals are collected from an atmospheric-pressure plasma jet (APPJ) for both nanosecond- and femtosecond-duration laser excitation pulses.

15. SUBJECT TERMS
atmospheric pressure plasmas; TALIF; femtosecond; nanosecond; atomic oxygen

16. SECURITY CLASSIFICATION OF:			17. LIMITATION OF ABSTRACT:	18. NUMBER OF PAGES	19a. NAME OF RESPONSIBLE PERSON (Monitor)
a. REPORT Unclassified	**b. ABSTRACT** Unclassified	**c. THIS PAGE** Unclassified	SAR	33	James D. Scofield 19b. TELEPHONE NUMBER *(Include Area Code)* N/A

Table of Contents

List of Figures

List of Tables

1. Introduction

Over the past decades the continuously evolving field of plasma physics has taken a number of leaps forward with regard to new plasma technologies. One area that has recently experienced significant growth is the development of highly non-equilibrium, low-temperature plasma sources operating in near-atmospheric pressure gas, and liquid environments [Samukawa et al. 2012]. These plasma sources are being explored in various configurations for a number of different applications that range from plasma-assisted combustion to materials processing to biomedical areas. While many of these sources are in the initial stages of development, all of the applications share an interest in understanding the spatial distribution and temporal evolution of key intermediate plasma species, including ions, neutral metastable, and reactive species [Ono 2016]. Atomic neutrals, such as hydrogen, oxygen, nitrogen, and carbon, are particularly important to quantify since they are both highly reactive and can be generated in significant concentrations. Absolute-concentration measurements of important intermediate plasma species in non-equilibrium plasmas provide key insights into understanding the physical and chemical nature of these plasma systems and facilitate the development of model-based predictive capabilities.

Diagnostic techniques used to quantify intermediate plasma species ideally should be non-intrusive, *in situ*, and species-selective, with a large dynamic range to permit the detection of low densities of reactive (short-lived) species, while avoiding saturation effects at higher densities. Traditional cw diode-laser and ns-laser-based spectroscopic techniques exhibit fundamental limitations despite providing a non-intrusive, in-situ species-selective measurement platform. For example, line-of-sight absorption spectroscopic techniques often lack sufficient spatial resolution. Laser-induced fluorescence (LIF) is based upon single-photon absorption and offers high spatial resolution; however, because of relatively strong absorption cross-sections, large concentrations can prove to be optically thick, resulting in significant probe-beam attenuation or stimulated-emission effects [Eckbreth 1996]. In addition, many key intermediates such as atomic hydrogen, oxygen, and nitrogen have a large energy spacing between the initial and excited electronic states. Such large energy spacings require high single-photon energies with wavelengths in the vacuum-ultraviolet (VUV) region, which is relatively difficult to generate and poses significant difficulty for propagation through air.

To address these complications, multi-photon excitation has been developed and employed. Multi-photon approaches offer two significant advantages: 1) Red-shifted excitation wavelengths from the VUV region allow beam propagation with minimal absorption in air and 2) smaller absorption cross sections enable high-resolution atomic species measurements at high concentrations. Two-photon-absorption laser-induced fluorescence (TALIF) was first demonstrated for atomic hydrogen and deuterium by Bokor et al. [1981] and has since been dramatically expanded to detect many other atomic ground-state species, including oxygen [Bischel et al. 1981, Aldén et al. 1982, DiMauro et al. 1984] and nitrogen [Bischel et al. 1981]. Studies conducted by the Miller group [Preppernau et al. 1989, Tserepi et al. 1992, Preppernau et al. 1995], the Döbele group [Niemi et al. 2001, Döbele et al. 2005] and others [Amorim et al. 1994, Czarnetzki et al. 1994, Amorim et al. 1995, Miyazaki et al. 1996, Boogaarts et al. 2002,] have significantly expanded TALIF as a diagnostic method for non-equilibrium plasma research.

Traditionally, nanosecond laser systems have been employed to probe TALIF transitions utilizing numerous excitation schemes. However, the relatively high fluence of typical nanosecond-laser pulses utilized to overcome the relatively small multi-photon absorption cross section can result in significant interference from photo-dissociation and photo-ionization within the medium. These sources of photolytic interference can be significant and permit quantitative measurement in a narrow range of laser fluence without requiring more sophisticated analysis techniques. To circumvent this problem, ultrafast (picosecond) lasers have been used in place of nanosecond systems. These high-peak-intensity, ultrafast excitation schemes are capable of producing signals that are similar to those of comparable nanosecond systems with significantly lower total power [Settersten et al. 2002, Frank et al. 2005, Kulatilaka et al. 2007, Kulatilaka et al. 2009]. The low average power of the ultrafast system limits photo-dissociation [Kulatilaka et al. 2008, Kulatilaka et al. 2009]. These efforts have recently been extended into the femtosecond regime [Kulatilaka et al. 2013, Kulatilaka et al. 2014]. This innovation generally enables higher signal intensities

with less photolytic interference, which yield several benefits over traditional TALIF techniques. In the current work, we demonstrate the merits of applying the fs-TALIF technique for measurement of atomic oxygen in an atmospheric pressure plasma jet (APPJ) source with a helium-oxygen feed-gas, through a direct comparison with conventional ns-TALIF. High-pressure microplasma sources provide an ideal testbed for this comparison. The small characteristic length scales typical of many microdischarge sources can yield strong spatial concentration gradients for atomic species on the order of 100 μm or less. Collisional quenching of excited states can also occur on sub-ns to single-ns timescales, pushing the limits of accurate calibration of ns-TALIF techniques. We show that the benefits of fs-TALIF over ns-TALIF include an overall greater excitation efficiency, the ability to directly measure excited-state quenching rates that are *detector-bandwidth-limited* rather than laser-pulse-width limited, higher dynamic range through a reduction in single-shot detection limits, the potential for two-dimensional imaging of atomic species, reduced interference from photo-dissociation, and higher precision calibration enabled by significantly reduced fluctuations in laser pulse energy that are characteristic of all-solid-state femtosecond laser systems.

2

2. Experimental

2.1. Atmospheric-pressure plasma jet details

The microdischarge source under study is a pulsed APPJ arranged in a capillary dielectric barrier discharge (CDBD) configuration. In this configuration, an active discharge with peak currents ranging from tens of mA to >1 A can be sustained outside the capillary and generate high atomic oxygen densities over the entire gap. The source is described in detail elsewhere [Sands et al. 2013] and is shown in Figure 1a. Briefly, the CDBD source consists of a 3 mm quartz capillary tube with an inner diameter of 2 mm. A 2-cm wide copper foil electrode, placed 5 mm behind the tip of the quartz tubing, is wrapped around the tube and is attached to the positive high voltage lead from a pulsed power supply. UHP (99.999%) helium is mixed with admixtures of UHP oxygen (mole fractions between 2% and 4%) inside a delivery line 2 m long to ensure homogeneity. The gas mixture flows through the quartz capillary tube and is directed downward towards a 3.4-cm diameter stacked aluminum-Teflon® cathode that is grounded through a 500 Ω resistor. The gas flow rates are controlled with MKS flow controllers accurate to within 1% of its full scale reading. The entire discharge system is mounted on a support structure that could be translated in three dimensions for diagnostic alignment purposes. The unipolar pulsed power supply generating the ns-rise-time voltage pulses was built with a stacked MOSFET switch (Behlke HTS-150) in a high-side configuration that is supplied with high voltage from a Glassman DC power supply. In the present configuration, a +11.0 kV peak voltage pulse train, with a 20-ns rise-time and 8-μs fall-time, is supplied to the anode at a pulse repetition rate up to 15 kHz. The fast rise-time of the voltage pulses allowed the discharge to be initiated with a higher reduced electric field. Consequently, the resultant DBD could be sustained with oxygen admixtures up to 5%. Applied voltage and current traces for each test were recorded with a Northstar 1000:1 high voltage probe connected at the anode, and a Pearson inductive current probe on the line from the cathode to ground, respectively. Current measurements were averaged over several hundred pulses. Typical averaged applied voltage and discharge current traces are shown in Figure 1b, for a 2% O_2/He mixture discharge over a 10 mm gap. Discharge power was determined from the electrical measurements as described in [Sands et al. 2013]. The laser systems used in this study were not co-located, so some variation in the discharge parameters can be expected since two different CDBD sources were necessary for testing. The configurations of these sources, however, were identical. The measured discharge power was used as a benchmark for comparing the state of the discharge under similar operating conditions.

(a)   (b)   (c)
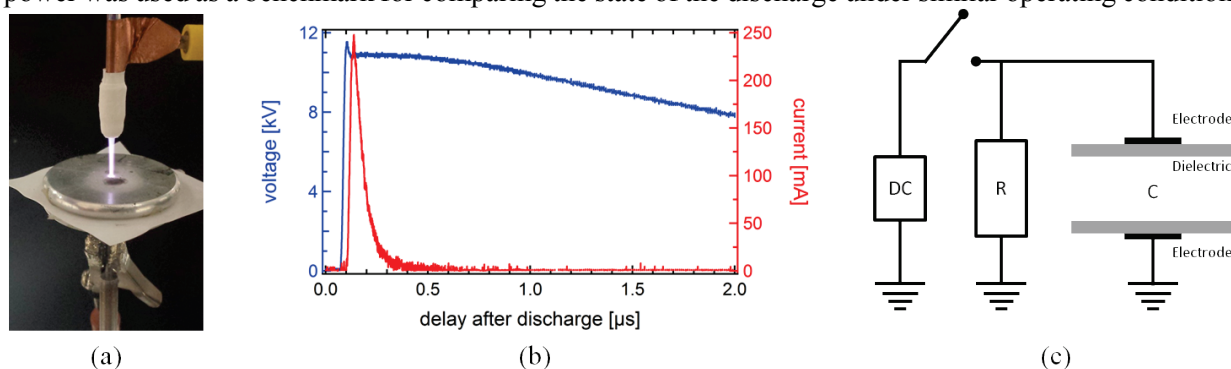
Figure 1: (a) Photograph of cDBD. (b) Applied voltage and current traces collected from a dielectric barrier discharge in a 2% O_2/He mixture over a 10 millimeter gap at atmospheric pressure. (c) Schematic of APPJ electrical circuit.

2.2. Laser diagnostic details

The fs-laser system used for atomic oxygen and xenon excitation near 225 nm consists of an optical parametric amplifier (Coherent, OPerA) pumped by a Ti:sapphire-based regenerative amplifier (Spectra-Physics, Solstice). The OPA, operating at a 1 kHz repetition rate, was able to deliver 24.7 μJ per pulse at 225.6 nm.

3

The ns-TALIF diagnostic system is based on a neodymium-doped yttrium aluminum garnet (Nd:$Y_3A_{l5}O_{12}$) (Nd:YAG) (Spectra-Physics, PRO-250) laser system. It is optically pumped at 10 Hz to produce 1064-nm wavelength output with 8 ns laser-pulse durations. This fundamental output is then frequency-tripled by mixing frequency-doubled output with the fundamental in a thermally stabilized beta barium borate (BBO) crystal. The 532-nm, 0.2 cm^{-1} linewidth residual from the frequency mixing process is used to pump a dye laser (Continuum, ND6000). The dye laser operates with a mixture of Rhodamine 640 (R640) and Sulfur-Rhodamine 640 (SR640) dyes in a methanol solvent. Very small amounts of Creysl Violet 670 (CV670) dye are added at the very end of the dye-mixing process to increase the total dye laser output. Amplified spontaneous emission (ASE) was less than 3% of the total dye laser output ensuring proper narrow-band operation of the dye laser.

The output of the dye laser and the frequency-tripled output of the Nd:YAG laser are down-collimated, spatially and temporally overlapped with a dichroic mirror and a manual delay stage, and mixed in a BBO crystal that was not thermally stabilized. The mixing produced the UV wavelengths required for the atomic oxygen and xenon TALIF studies. In order to help balance the output energy of the dye laser and the third harmonic, the frequency-tripling process was slightly de-tuned. When done correctly, this affected neither the mode shape nor caused distortion of the output beam shape. The UV mixing output could be frequency-tuned by scanning the grating of the dye laser. This, as well as the manual delay stage on the third harmonic Nd:YAG output, was adjusted to ensure resonance with the specific transition as well as produce peak TALIF signal. The UV output from the BBO mixing process was spatially separated with a Pellin-Broca prism.

The output from either the fs or ns laser systems was passed through a 160 μm thick, uncoated UV-fused silica pick-off window and focused with a 50 mm UV fused silica lens into the collection volume. The pick-off window directed a calibrated amount of the laser energy to a pyro-electric detector (Ophir, PD-9), which was used to simultaneously measure shot-to-shot laser power during TALIF signal collection. These data were used to correct the TALIF signal on a shot-to-shot basis instead of measuring an average power, and was done to help ensure the accuracy of the measurement. For the ns-TALIF measurement, this is especially critical as there are many laser components used to generate the required UV photons which can cause large shot-to-shot fluctuations. In multi-photon excitation, these fluctuations have a much more significant impact on the accuracy of the data compared with single-photon laser-induced fluorescence, due to the quadratic dependence of the TALIF signal on laser intensity.

Two different optical systems were used for fs-TALIF and ns-TALIF signal detection. The ns-TALIF signal detection system had higher collection efficiencies, but was limited to a 10 Hz repetition rate. The fs-TALIF system had lower collection efficiency, but enabled much faster data collection. Only when a direct comparison between fs-TALIF and ns-TALIF signals were made was the same detection system used.

The detection system consisted of two main parts; a camera used to image the TALIF signal in the discharge volume of the APPJ, and a gated photomultiplier tube (PMT) used to make point-based collisional decay measurements of the laser-pumped excited electronic state.

The high-speed camera system used for fs-TALIF imaging consisted of a CCD (Andor Newton^{EM}) camera coupled with a gated intensifier (LaVision IRO). A total gate time of 200 ns was used to collect the fluorescence signal, the repetition rate of the external intensifier was set at 1 kHz, and it acted as a shutter for the CCD camera that had an exposure time of 0.1 sec. The 10 Hz imaging system used for ns-TALIF imaging utilized an intensified charge-coupled device (ICCD) camera (Princeton Instruments, PIMAX) One hundred total images were collected for each data point. Both imaging systems utilized a pair of 50 mm f/1.4 Nikkor lenses, and a 2" diameter band-pass filter centered at 840 nm. The two lenses were used in a conjugate imaging arrangement to help maximize the collection solid angle. With an in-band transmission of over 95% and an out-of-band optical density of over 6.5, the filter was well suited for collection of the fluorescence from the atomic species and fluorescence from the calibration gas while rejecting laser scatter and emission from the plasma. The spatial resolution of each imaging system was ~25 μm/pixel. The CCD was electronically cooled to -80°C to reduce dark-current noise. A "best-case" signal-to-noise ratio (SNR) of 60:1, with a typical value of 25:1, was obtained.

Depending on the laser system, the PMT used was either a high-voltage gated PMT socket and side-on PMT tube (Hamamatsu, R1477-06) with slower (2 ns) response times, or fast-response (500 ps) high-voltage gated end-on PMT (Hamamatsu, H1156-20-NF). The higher bandwidth PMT allowed for sub-ns collisional quenching measurements using the fs-TALIF system. The gated PMT systems were used to help discriminate against the longer lived plasma emission and collect only the TALIF signal. A home-built circuit was designed to set gain to the H1156-20-NF PMT. An identical band-pass filter was used on each PMT collection system. A multi-lens system was used for collection of the TALIF signal for the PMT. 2" diameter lenses were used to maximize the solid angle for collection, with additional coupling lenses selected to match the numerical aperture of the fiber passing the signal to the PMT to minimize signal loss.

Only fast-impulse-response time PMTs were used for all fs-TALIF measurements. Depending on background light levels, either a gated (Hamamatsu R1046U-50) or non-gated (Hamamatsu R1156) PMT was used for point-based collisional quenching rate measurements. Both offer much shorter impulse-response times compared to the 2-ns response time of the R1477-06 used in the ns-TALIF measurements, 200 ps and 500 ps, respectively, and allow sub-ns collisional quenching measurements to be made. The gated-PMT system was used to help discriminate against the weaker, longer-lived plasma emission and collected only the TALIF signal, whereas the non-gated PMT could be used in calibration when background emission was non-existent. Additionally, both the R1046U and R1156 had very similar collection efficiencies and signal gain factors compared to the R1477 PMT used in the ns-TALIF measurements. The PMT used was fitted with the same band-pass filter as used in the imaging discussion above and the same three-piece relay lens system discussed above in the ns-TALIF PMT discussion was used to maximize the solid angle for collection and minimize signal loss.

2.3. Noble gas calibration

Quantification of the atomic-species number density is necessary for applications where TALIF is used and requires accurate calibration of the detection system. A number of calibration techniques have been used, ranging from known-concentration reference sources [Clyne et al. 1979] to single-photon-absorption methods [Amorim et al. 1994] to manual evaluation from first principles, based on known parameters of pump laser system, interaction volumes, cross-section, and signal collection. These methods have proved to be difficult because of their rigorous nature, small absorption cross-sections, or lack of comparable absorbers. Two more common calibration techniques are NO_2 titration and noble-gas calibration. For NO_2 titration, often used for H-atom TALIF calibration, a known quantity of NO_2 is introduced into the optical detection region where it quenches the atomic hydrogen via a fast, single-step reaction [Meier et al. 1990]. The addition of NO_2 can be done at different pressures, temperatures, and volumes to determine the linear relationship with the total atomic hydrogen number density present before titration. While very accurate, this method can be difficult to implement, especially in a short discharge pulse duration, without affecting the bulk discharge properties.

Noble-gas calibration, which has become a more commonly used technique, is easier to implement when available, and relies on excitation and fluorescence characteristics that are similar to those of the atomic species being calibrated [Niemi et al. 2001, Dobele et al. 2005]. This method starts by normalizing the total measured fluorescence signal by the square of incident laser intensity, integrated over space and time. When the ratio of flux-normalized fluorescence from the test gas to that of the noble gas used for calibration is determined, many of the parameters drop out. This leaves the expression given in Eqn. 1 which relates the unknown number density of the atomic species, n_X, to the known number density of the noble gas, n_{Cal},

$$n_X = \frac{\eta_{Cal}}{\eta_X} \frac{\Phi_{Cal}^2}{\Phi_X^2} \frac{a_{Cal}}{a_X} \frac{\sigma_{Cal}^{(2)}}{\sigma_X^{(2)}} n_{Cal} = \chi \frac{S_X}{S_{Cal}} n_{Cal} \qquad \text{Eqn. 1}$$

This relationship is derived from the collision-free case, where quenching is not directly accounted for and includes relative detector sensitivities η, incident laser fluence $\Phi_i = \dfrac{T_i E_i}{h A \upsilon_i}$ (composed of optical attenuation factor, T_i, measured laser pulse energy E_i, area of incident beam A, and laser frequency υ_i), effective branching ratio of the observed fluorescence a_i, two-photon absorption cross-sections $\sigma_i^{(2)}$, and observed fluorescence intensities S_i. This equation assumes that collection parameters such as solid angle, gain, and exposure durations are held constant during the calibration and fluorescence-collection measurements.

If the gas is at a very low pressure and can be assumed to be collisional-less, the calibration factor would depend only on atomic cross-sections and experimental constants. However, at high pressure (>5 Torr, depending on mixture conditions), additional corrections must be made. As pressure is increased, collisions between the excited atoms and other species become more significant, resulting in increased non-radiative (collisional) energy transfer and reduction of the fluorescence intensity. Essentially, collisional quenching reduces the effective branching ratio of a spontaneous transition from state i to state k. This is shown in Eqn. 2 where A_i is defined as $A_i = \sum_{k<i} A_{ik} = \dfrac{1}{\tau_i}$ and denotes the total spontaneous emission rate of the excited state.

$$a_{ik} = \frac{A_{ik}}{A_i} \xrightleftharpoons[\downarrow P]{\uparrow P} \frac{A_{ik}}{A_i + Q_i} \qquad \text{Eqn. 2}$$

$$a_{ik} = \begin{cases} \dfrac{A_{ik}}{A_i} & P < 5\,Torr \\[2ex] \dfrac{A_{ik}}{A_i + Q_i} & P > 5\,Torr \end{cases}$$

The effective quenching rate is defined as $Q_i = \sum_q k_q^i n_q$, i.e. the sum of the product of the number density of the quenching species, n_q, and its corresponding quenching coefficient, k_q^i.

The effective quenching coefficient is measured by directly monitoring the fluorescence decay in both the plasma jet and separate calibration gas using PMTs as discussed in Section 2.2. An example ns-TALIF signal is shown in Figure 2. The observed signal decay is a convolution of the natural radiative rate, the net effective quenching rate, and the excitation rate of the excited state, given by the square of the measured laser pulse intensity. Since two of these components, the excitation rate and the natural radiative decay rate, are known, the effective quenching rate can be inferred through fitting. This method has been demonstrated previously for ns-TALIF [van Gessel et al. 2013] with good accuracy.

Approved for public release. Distribution is unlimited.
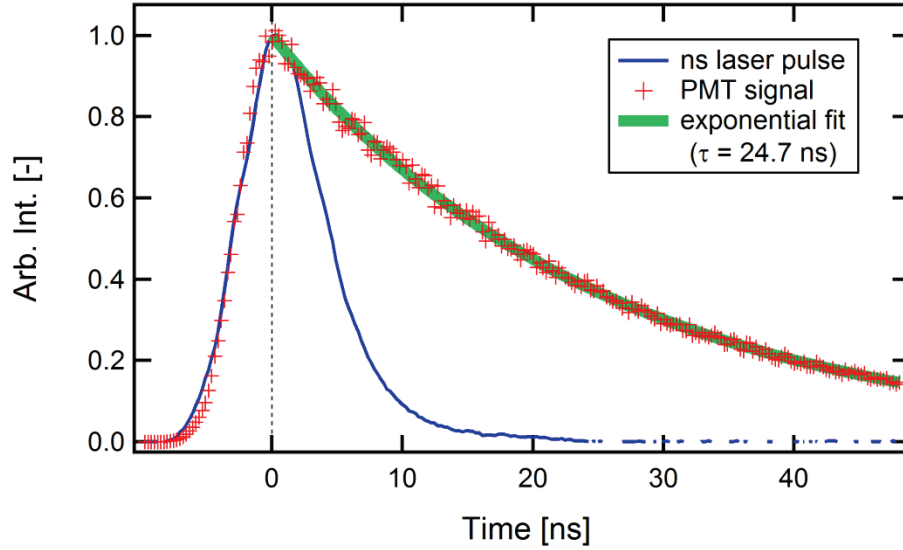
Figure 2: Plot illustrating ns-TALIF quenching measurements, showing fluorescence decay curve, exponential fit, and laser pulse waveform.

In order to perform this correction, the same PMT is used to monitor the incident laser pulse shape and the resultant fluorescence. These do not have to be collected simultaneously, and absolute scale is not important for these measurements. It is important for the collected signal magnitude to remain within the linear-response regime of the PMT. The laser pulse trace is squared, since TALIF signal scales linearly with squared laser energy, normalized, and plotted together with the normalized TALIF trace. This requires the leading edges of both waveforms to coincide in time and assumes that internal conversion of the excitation energy into fluorescence is an instantaneous process. In actuality, this is not true and can occur over several picoseconds depending on conditions. However, the impulse-response time of the PMTs are sufficiently slow to justify this assumption. The best fit of the TALIF data has the form given in Eqn. 3, where $\frac{1}{\chi}$ is the normalization constant, $S_L(t)$ is the laser signal, and τ_{eff} is the effective decay time.

The effective decay time is composed of both the natural radiative lifetime, τ_{NL}, and the first order quenching lifetime, $\tau_{Q^{(1)}}$, as shown in Eqn. 4.

$$\frac{1}{\chi}\left[\int_0^t \left[S_L(t)\right]^2 dt\right] \cdot \exp\left[-\left(\frac{t}{\tau_{eff}}\right)\right] \qquad \text{Eqn. 3}$$

$$\tau_{eff} = \frac{\tau_{NL}\tau_{Q^{(1)}}}{\tau_{NL} + \tau_{Q^{(1)}}} \qquad \text{Eqn. 4}$$

Second order quenching is neglected for these fluorescence measurements as the two-photon transition is not saturated. It is important to note that the fitting accuracy is critically dependent on the recorded pulse shapes.

Using this procedure, the fluorescence decay rate is obtained over a range of pressures. A linear relationship between the concentration of the quenching species and the fluorescence decay rate is obtained that takes the form shown in Eqn. 5.

$$\tau_f = \tau_{NLF} + k_Q[Q] \qquad \text{Eqn. 5}$$

For noble-gas calibration of atomic-oxygen concentrations, xenon was selected since the $5p^6$ $^1S_0 \rightarrow 6p'[3/2]_2$ transition of Xe lies very close to the $2p^4\ ^3P_{2,1,0} \rightarrow 3p\ ^3P_{1,2,0}$ transition of oxygen. These transitions are shown in Figure 3.
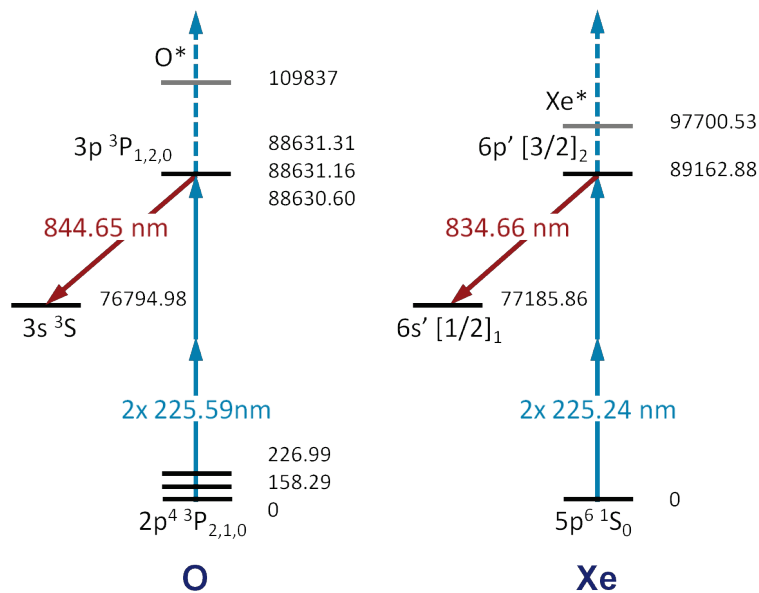
Figure 3: Energy level diagrams for two-photon excitation of oxygen and xenon. Energy is shown in wavenumbers at the right of each graphic.

The lower O $2p^4\ ^3P_J$ and upper O $3p\ ^3P_{J'}$ states in atomic oxygen are divided into three levels with orbital angular momentum quantum numbers J = 2, 1, 0 and J' = 1, 2, 0. While the upper states are very closely spaced and cannot be distinguished during laser excitation or fluorescence, the spacing between the lower states is much larger. Because the population of each of these levels follows a Boltzmann distribution, which is dependent on local gas temperature, conventional ns-duration laser-based diagnostics require knowledge of either the relative population distribution between the three sublevels or the local temperature. Usually, the population distribution for each of the sublevels is determined by scanning over each of the lower levels individually, at 225.685 nm, 225.988 nm, and 226.164 nm. The total atomic oxygen ground-state density is then determined by summing all of these J-level number densities. In contrast, the large bandwidth of the fs laser pulse (>1.2 nm FWHM) allows simultaneous excitation from all three sublevels. Each of the individual J-sublevel excitations must be normalized against the incident laser intensity at that wavelength, but requires neither scanning of the laser wavelength nor knowledge of local gas temperature. Once normalized, the collected fs-TALIF signal does not need to be additionally corrected as all J sublevels are simultaneously excited and fluoresce during the single collection sequence. Figure 4 shows the calculated relative two-photon absorption cross-sections for each of these specific transitions [Saxon et al. 1986] and are used when making relative comparison between different excitation schemes during the TALIF measurements.

0 88631.32

3p ^{3}P 2 88631.16

J' = 1 88630.60 cm^{-1}

0.561 0.00 0.088

0.439 0.329 0.714

0.00 0.671 0.198

0 226.99

2p^4 ^{3}P 1 158.29

J = 2 0 cm^{-1}
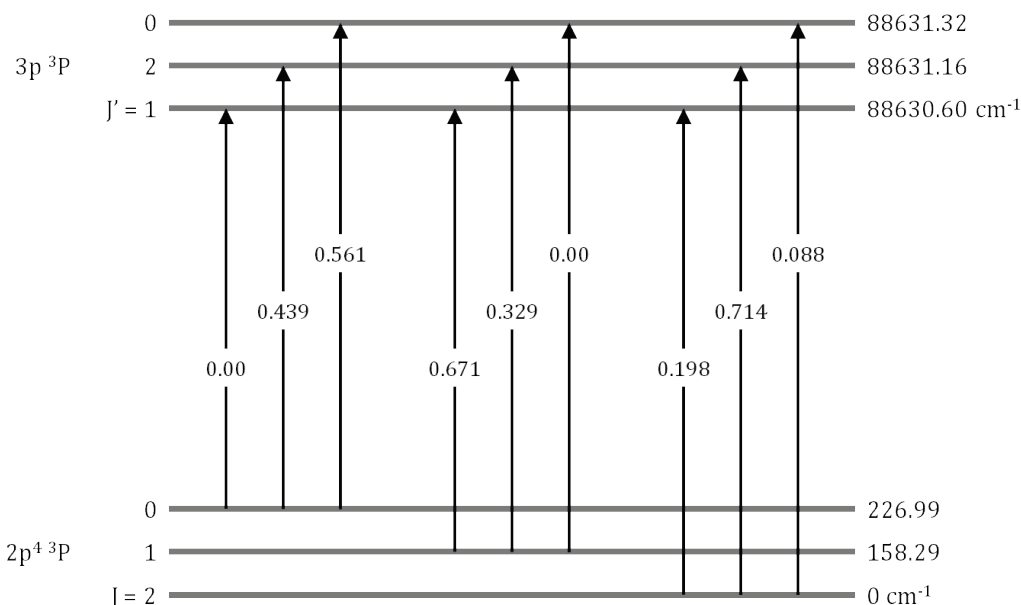
Figure 4: Atomic oxygen transition probabilities from each J sublevel for the 2p^4 ^{3}P $\rightarrow$ 3p ^{3}P transition.

2.4. Quenching-relevant parameters

The calibration of fs-TALIF data was performed in a low-pressure cell, at a non-flowing condition, when the cell was evacuated to 0.01 Torr total pressure and then backfilled with the xenon gas. Four sequences of TALIF images of the calibration gas were acquired at pressures ranging from 0.3–25 Torr and the cell was re-evacuated. Each calibration sequence collected Xe-TALIF from ten arbitrarily selected pressures, starting from a lower pressure and steadily increasing. The entire calibration required less than 15 min to perform. With a measured leak-up rate of < 5 Torr per hour at 1 Torr, the cell was assumed to be filled with pure calibration gas for the duration of the calibration.

Quenching rates were collected over a wide range of pressures to obtain natural lifetime of the excited state atomic species and the collisional quenching coefficients for specific quenchers. These plots are shown in Figure 5 for atomic oxygen in helium (left) and xenon in xenon (right). The ns-TALIF limit shown in Figure 5(right) is the limit that an 8 ns laser pulse would be able to accurately resolve based on the methodology discussed above. To help minimize the effect of temperature on the quenching rates obtained, the discharge was operated at a low pulse energy condition and long integration times were used to help improve signal-to-noise ratios. The rates obtained from each of these tests are summarized below in Table 1 and are compared against data found in the literature. In general, the rate constants determined from the present experiments are in agreement with the literature. However, it is assumed that the present experimental data are more accurate due to a wider pressure range over which they were obtained.
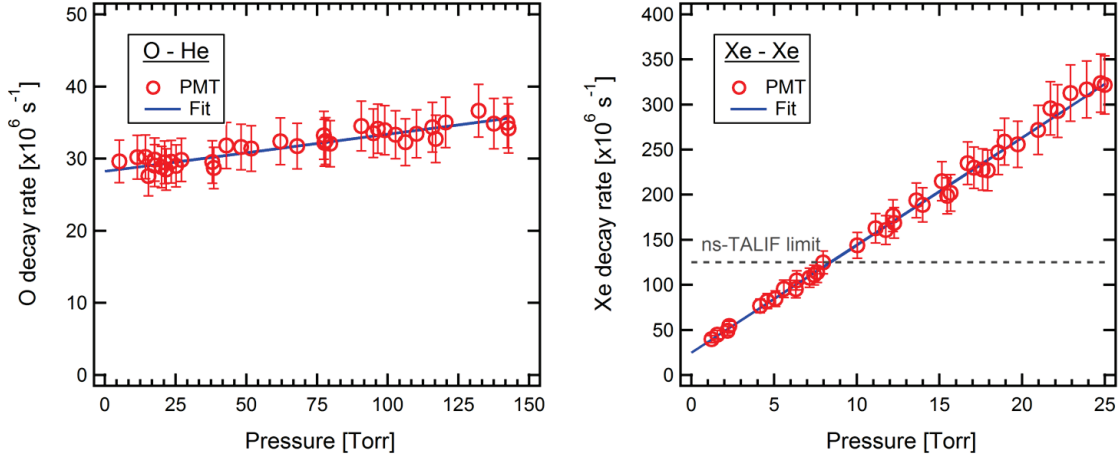
Figure 5: Stern-Volmer plots generated to determine quenching rate constant and natural lifetime for atomic oxygen in helium (left) and xenon in xenon (right).

For the ns-TALIF results presented in this work, quenching-relevant parameters were calculated from previously published works (partial quenching rates of O-He, O-N$_2$, and O-O$_2$). These values for two-photon absorption cross section, natural lifetime, and species-specific quenching coefficients are summarized in Table 1. For the fs-TALIF results presented here, an effective quenching rate was directly measured. While not discriminating between the possible quenching species, the fs-TALIF quenching results, presented below, show significantly increased accuracy at these working pressures, as shown in Figure 5(right).

The calibration of ns-TALIF data followed a similar procedure to that described by Van Gessel et al., which used xenon gas added directly to the unpowered helium jet for signal calibration [Van Gessel et al. 2013]. In this method, effective branching ratios a_{Xe} were precisely measured using known mixture ratios of helium and xenon at atmospheric pressure. To apply the published a_{Xe}, measured with a xenon concentration in helium of 3.5%, the Xe-TALIF signal was measured with Xe/He admixtures in the range of 10-20% and extrapolated to 3.5% using a linear fit in order to match the conditions of measurement. Because direct quenching measurements could not be derived from the TALIF signal for O$_2$/He admixtures > 0.5%, literature values of rate coefficients from Table 1 were used instead.

Table 1: Two-photon absorption cross-sections, $\sigma^{(2)}$, natural lifetimes, τ, quenching coefficients, k_i, and fluorescence quantum yields, a_{21}, for atomic oxygen and xenon excited states at 300 K.

		O (3p $^3P_{1,2,0}$)	Xe (6p'[3/2]$_2$)
$\sigma^{(2)}$ [cm^4]		$2.66\pm0.80 \times 10^{-34}$ [a]	$4.94\pm0.98 \times 10^{-34}$ [b]
τ [ns]		35.4±1.4* 34.7±1.7 [b] 35.1±3.0 [e] 36.2±0.7 [f]	40.0±1.6* 40.8±2.0 [b] 40±6 [c] 37±2 [g] 30.7±2.2 [h]
k_i [10^{-10} cm^3 s^{-1}]	O$_2$	8.6±0.2 [a] 9.4±0.5 [b] 9.3±0.4 [e] 6.3±0.1 [f]	
	He	0.016±0.002* 0.017±0.002 [b] 0.07±0.02 [e] 0.15±0.05 [f]	5.7±0.3 [h] 5.7±0.6 [c] 9.3±2.0 [i]
	N$_2$	5.9±0.2 [b] 4.3 [f]	5.1±0.45*
	Xe		3.7±0.14* 3.6±0.4 [b] 4.2±0.5 [c] 4.3±0.1 [d]
a_{21}	He	0.22-0.054*	
	Xe		0.27*

* This study, [a] Bamford et al. 1986, [b] Niemi et al. 2005,
[c] Alekseev et al. 1996, [d] Bruce et al. 1989, [e] Niemi et al. 2001,
[f] Bittner et al. 1988, [g] Inoue et al. 1984, [h] van Gessel et al. 2013,
[i] Zikratov et al. 1996.

3. Results and Discussion

To determine the overall excitation efficiency for both laser systems, the TALIF signal for each system must be compared. To do this, peak signal was collected for each system from the centerline of the APPJ operating at the same conditions. For this comparison, operation in a 0.5% O_2/He mixture was selected. This kept the mole fraction of added O_2 as small as possible to ensure O_2-based collisional quenching lifetimes were longer than both laser pulse widths, but still above detection limits. This is significant for this comparison as multiple excitation events would negatively impact the comparison. For this mixture, $1/e$ quenching measurements collected 0.5 mm under the anode were ~8.5±0.15 ns after accounting for radiative decay, providing grounds to preclude multiple excitation events as an issue. The probability of re-excitation for the fs-duration laser pulse is significantly lower, since decay time for the excited state population, as well as dephasing period are significantly longer than the FWHM of the squared intensity of the fs-duration laser pulse. To mitigate differences between the two systems, the same camera system was used to collect both the fs-TALIF and ns-TALIF signal. Due to the higher quantum efficiency, the ICCD system described in Section 2.2 was used. Additionally, the TALIF signal was also collected with the fast-impulse-response time PMT to correct for collisional quenching. Each signal was collected under similar discharge conditions when all collection parameters, with the exception of laser pulse energy, were identical. For this comparison, both laser beams were focused down to a point with the same optical system and focal waist parameters were verified with a translated knife edge and beam profiling camera. Table 2 summarizes these parameters, which include number of averaged incident laser pulses per exposure, imaged signal area, quantum efficiency of the system, and solid angle for collection.

The 10 Hz ns-TALIF laser-diagnostic system used in the present work produced 8 ns duration pulses with energy peaking at 120 μJ. To avoid saturation and photo-ionization the laser was operated with a pulse energy of approximately 50 μJ. The laser beam was focused with a spherical lens to a focal area with an approximate diameter of 100 μm, producing an average power density of 6.4 W cm^{-2} and a peak power density of approximately 8.0×10^7 W cm^{-2}. The 1 kHz fs-TALIF laser-diagnostic system produced 100 fs pulses with energy peaking at 25 μJ, but was operated at approximately 12 μJ. When focused in to a sheet with dimensions of 2 mm by 90 μm, an average power density of 6.7 W cm^{-2} and a peak power density of approximately 6.7×10^{10} W cm^{-2} was produced. While conducting this comparison, the signal was calibrated and a quadratic relationship of the TALIF signal with incident laser energy was ensured. This shows the first significant advantage of the fs-laser system compared to the ns-laser system, i.e. at similar average power densities, the fs laser has a significantly higher peak power densities.

Table 2: Summary of parameters used to determine excitation efficiency of ns- and fs-based TALIF

	ns-TALIF	fs-TALIF
Averaged laser pulses per exposure	100	100
Imaged area dimensions	1 mm × 0.1 mm	1 mm × 0.1 mm
Spatial resolution (camera pixel)	25 μm	25 μm
Quantum efficiency of detection system	35%	35%
Solid angle	0.66 sr	0.66 sr
Average laser pulse energy	50 μJ	12 μJ

The square root of the background-corrected signal was normalized by the incident laser energy, to obtain a total signal per laser pulse. For these operating conditions, peak TALIF signals from the ns-laser system were around 1.24×10^4 counts, whereas the fs-TALIF signal strength peaked around 1.18×10^4 counts. Correcting these signals based on the parameters presented in Table 2 suggests that the fs-duration

pulse is ~15 times more efficient for exciting the given two-photon atomic oxygen transition, which enables full two-dimensional planar imaging. This suggests that the difference in excitation efficiency is purely due to the higher intensity of the fs laser pulse, since identical collection systems were used and the discharge was operated in a regime where quenching lifetime was limited.

3.1. Accuracy in quenching measurements

One of the most significant reasons for moving to sub-ns-based laser diagnostics is the ability to accurately collect excited electronic state collisional quenching data. Since the difference between the incident laser intensity profile and measured decay must be taken into account to obtain accurate quenching rates, many applications of TALIF diagnostics have been conducted under conditions where excited-state decay times are longer than the incident laser pulse. However, when this is not the case and decay times are on the order of the incident laser pulse or faster, accurate de-convolution of the measured decay rates becomes much more complicated, if not impossible. This is demonstrated in Figure 6 for atomic oxygen ns-TALIF signal collected 1 mm from the tip of the anode in a 2% O_2/He mixture APPJ discharge. For this condition, the measured TALIF signal decay time matches the measured 8-ns- FWHM laser pulse intensity profile. In this limit, where the decay of TALIF signals are limited by the laser pulse bandwidth rather than the excited state effective lifetime, it is no longer possible to extract one from the other and assumptions must be made as to the collisional quenching rate in order to convert TALIF signal to ground-state atomic oxygen density.
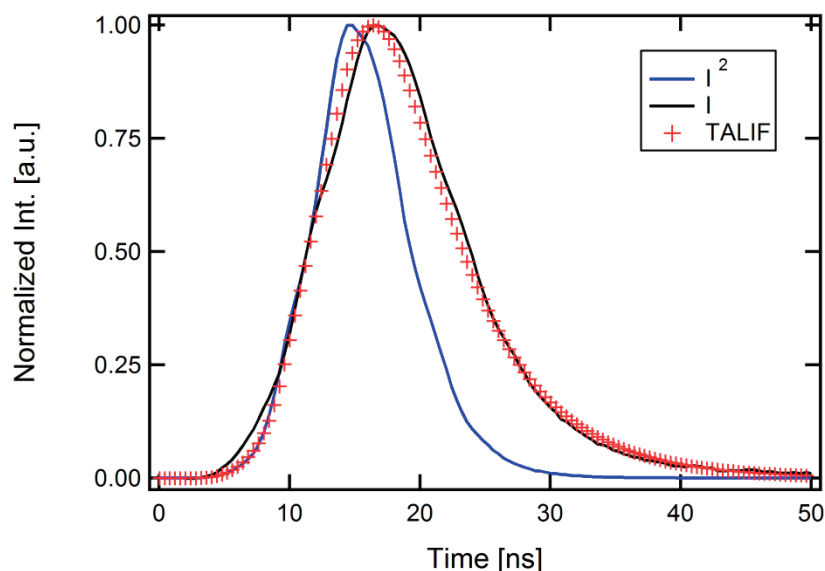
Figure 6: Atomic oxygen ns-TALIF signal collected from 2% O_2/He mixture APPJ discharge with fast impulse-response-time PMT and 8-ns FWHM laser pulse duration illustrating the limitations of ns-duration laser pulses to accurately resolve sub-ns excited-state effective lifetime.

Using a fs-TALIF technique, the advantages of directly measuring sub-ns excited-state decay times become apparent during an analysis of radially resolved fluorescence decay measurements in the APPJ. Figure 7(left) shows the atomic oxygen number density distribution in a 2% O_2/He mixture (from Figure 1a) and Figure 7(right) shows the radial distribution of atomic oxygen number density and fluorescence decay rates obtained by translating the detection optics coupled to the fast-gated PMT along the line shown at location A in Figure 7(left). The measured fluorescence decay times range from 7.3 ns on the centerline of the core flow to the limit of the PMT response time of 500 ps ~1.1 mm away from the centerline. These fluorescence decay times are below the response limit of the ns-TALIF system due to the 8-ns laser pulse duration and can only be measured with the fs-TALIF system. This can potentially improve the accuracy of atomic oxygen densities derived from the measured fluorescence signal, particularly in the case of APPJs,

where the entrainment of air leads to greater uncertainty in the relative mole fraction of colliding species as one progresses radially outward from the centerline.
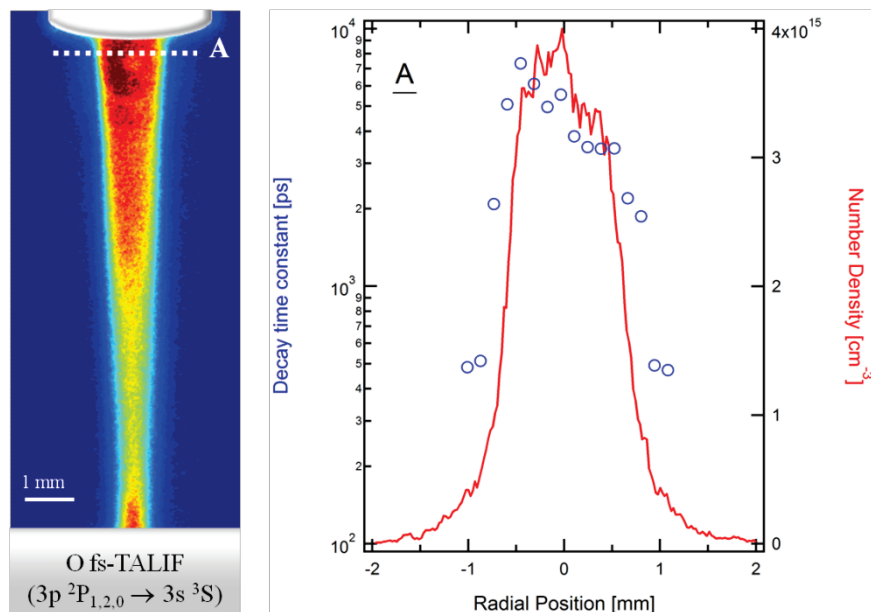
Figure 7: (left) Atomic oxygen number density distribution in a 2% O2/He mixture APPJ, collected 25 ms after voltage onset (from Figure 1). (right) Radial distribution of atomic oxygen number density at location A (shown on the left) compared against fluorescence decay time.

3.2. Laser power fluctuations

The architecture of an fs laser system is fundamentally different than that of a ns laser system. The most significant difference is that the fs laser system is mode-locked allowing for ultrashort pulse generation. Additionally, the fs-laser system is entirely based on solid-state gain media, compared to the solid-state and liquid dye gain media used in the ns-laser system. Lastly, there is better thermal stability built in to the fs laser system, including thermally stabilized Ti:sapp crystals and non-linear conversion crystal base plates. All these factors combine to reduce shot-to-shot laser energy fluctuations in the fs-laser system. Typical laser pulse energy fluctuations for 200 sequential laser pulses are shown in Figure 8 for both fs- and ns-laser systems. The standard deviation for these fluctuations is just over 2% of the operational level for the fs-TALIF system, whereas the standard deviation for the ns-TALIF system is nearly 10%. These fluctuations can be corrected for, but, as mentioned before, unless the incident laser energy is monitored and collected simultaneously with the TALIF signal, they introduce significant uncertainty in the measurements, depending on the system.
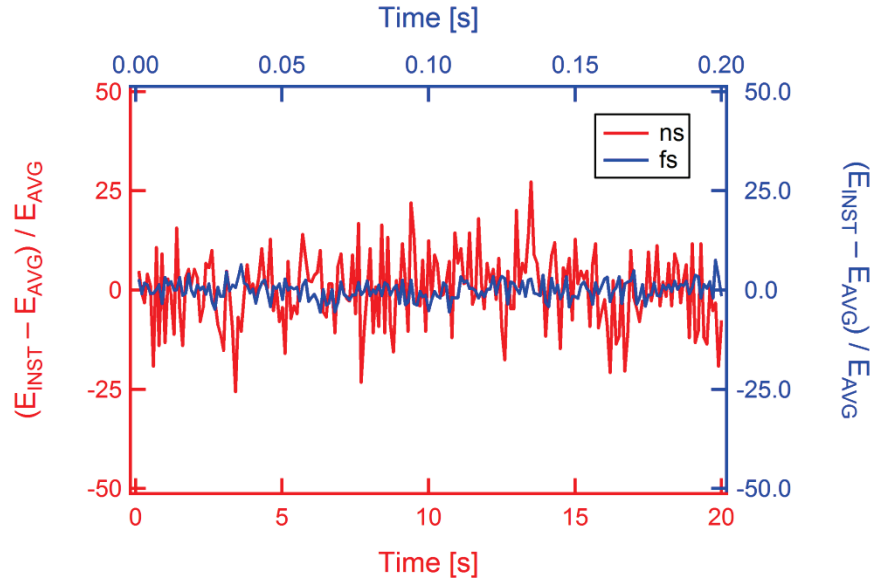
Figure 8: Normalized UV fs- (blue) and ns-laser (red) system pulse energy fluctuations for 200 sequential laser pulses during typical operation.

3.3. Reduced photo-dissociation

As discussed previously, one of the major limitations of ns-TALIF is the relatively large laser pulse energy required to produce moderate fluorescence signal. This average energy is capable of inducing photo-dissociation, which would artificially increase the atomic species number density. This effect can be seen in Figure 9, where radial profiles of atomic oxygen number density are collected for different incident laser energy levels, for both fs- and ns-TALIF, for the same 4% O_2/He discharge operating conditions. With 4% O_2 added, 11 kV applied voltage, and a pulse repetition frequency of 15 kHz, the He-O_2 discharge mostly produces ozone that enshrouds the plasma jet up to ~1 cm from the discharge axis [Sands et al. 2013]. At 226 nm, the cross-section for O_3 photo-absorption in the Hartley-Huggins band is more than 5 orders of magnitude larger than non-resonant continuum photo-absorption in O_2 [Molina and Molina 1986, Hasson and Nicholls 1971]. The normalized ns-TALIF radial profiles, shown in Figure 9a, show that as ns-laser pulse energy is increased, the radial profiles become increasingly perturbed by off-axis contributions to the O-atom TALIF signal. Since the collected TALIF signal is used in the noble gas calibration, photo-dissociation of ozone generated by the discharge artificially increases the calibrated atomic oxygen number density, reducing the accuracy of the measurement. This has been observed as a complication for O-atom TALIF measurements in atmospheric pressure discharges [Ono et al. 2009]. However, the fs-TALIF equivalents shown in Figure 9b for comparable average laser energies show no discernible effects from photo-dissociation. This is because, while the average incident beam energies are comparable, the peak energy flux or fluence for the fs laser system is significantly lower. Because photo-dissociation scales linearly with incident laser energy flux, the much lower peak fluence ensures photo-dissociation remains low and ensures the accuracy of the fs-laser system.

(a)   (b)
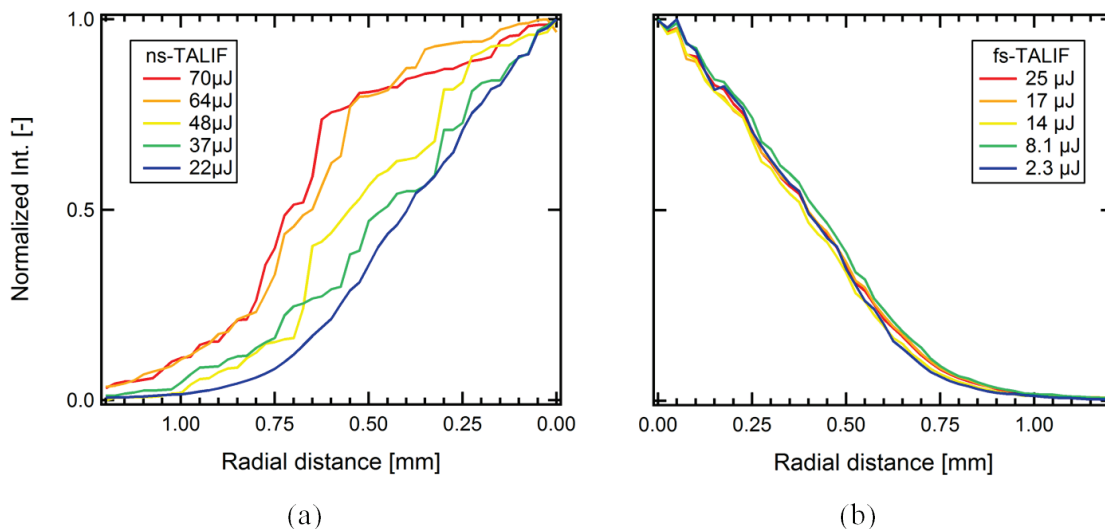
Figure 9: Comparison of induced photo-dissociation levels for different incident laser pulse energies indicated in the legend for (a) ns-TALIF and (b) fs-TALIF. Independent of incident energy, fs-TALIF shows no discernible levels of induce photo-dissociation.

### 3.4. Spatial homogeneity in planar imaging

Because the beam from the femtosecond laser system can be spread into a 2 mm sheet while maintaining at least the same power density to the spot-focused beam from the nanosecond system, this opens the possibility for reconstructing two-dimensional images of atomic species distributions much more effectively than was previously possible [Schmidt et al. 2015]. In order to compare the capability of the ns-TALIF and fs-TALIF systems for two-dimensional imaging, the APPJ was operated in an ozone-dominant (low discharge power) and atomic oxygen dominant production regime (high discharge power). The distribution of atomic oxygen changes significantly depending on which regime the discharge is operating in. Sequential images of TALIF emission were acquired by translating the laser beam along the discharge axis. The measured signals were then corrected based on quenching rates measured at a point and extrapolated to the rest of the two-dimensional image. This methodology was confirmed by collecting radially resolved quenching measurements at a number of different axial positions in the discharge. Not entirely surprising, the quenching rate proved to be relatively constant in these discharge locations other that near a composition gradient where quenching partners vary drastically. These occurrences are discussed in more detail in each subsection.

The image reconstructions with each CDBD operating in the atomic oxygen production regime are shown in Figure 10 for both ns- and fs-TALIF schemes. In each case, the discharge was operated with a 2% O_2 admixture and a pulse repetition rate of 15 kHz. Both ns- and fs-TALIF composite images have approximately 50% overlap between sequential line images (for ns-TALIF) and small sheet images (for fs-TALIF), respectively, such that vertical scanning to reconstruct the full image helped to minimize spatial variation. Laser power and background corrections were made to both sets of individual images and additional spatial corrections were made to the fs-TALIF images to correct for non-homogeneous laser sheet energy distributions. In this discharge regime, a high average power is dissipated in the discharge volume, 4.5 W in the case of the fs-TALIF CDBD and 4.3 W for the ns-TALIF CDBD. This results in a filamentary discharge along the flow axis, producing relatively high densities of atomic oxygen compared to operation below the turnover frequency, and shows relatively little radial structure. Comparison between the two reconstructed images reveals significant differences in spatial distributions. Specifically, in the axial direction, the fs-TALIF image shown on the right in Figure 10 displays much more uniform atomic oxygen TALIF signal distribution and smoother overlap between sequential raw TALIF images compared to the ns-TALIF image on the left.

16
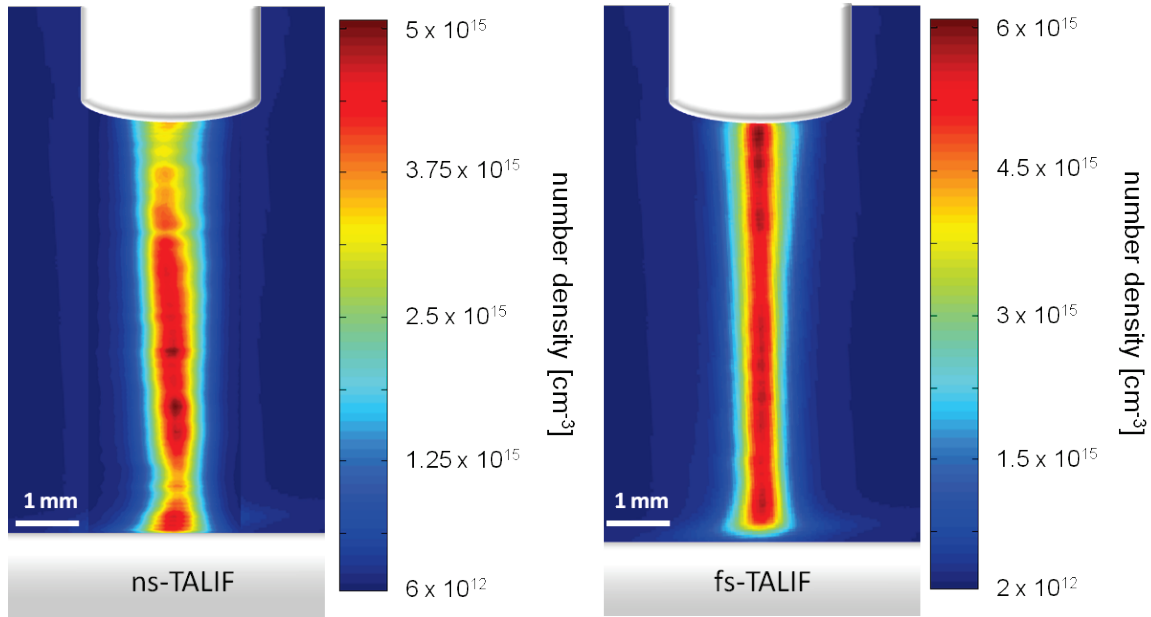
Figure 10: Comparison between ns-TALIF (left) and fs-TALIF (right) two-dimensional images for the same discharge in a 2% O₂/He mixture APPJ. fs-TALIF minimum detection limit are shown to be a factor of three lower while measured peak concentration is only 9% higher than corresponding ns-TALIF measurements.

The atomic oxygen distribution in the axial dimension is expected to be much more uniform than the ns-TALIF image implies. Volume-averaged emission images from the helium (3s ^{3}S → 2p ^{3}P) line are taken at the same operating conditions, which appears axially uniform and suggest the same. These results are shown in Figure 11 and show that the atomic oxygen number density distribution measured by the fs-TALIF diagnostic system and helium emission both remain relatively flat between anode and cathode and do not show local minima or maxima with the magnitude comparable to that shown in the ns-TALIF image in Figure 10(left). One of the main differences between the two composite images is the total collection time. Since the fs-based laser system afforded planar imaging at a 1 kHz repetition rate, the total time taken to construct the full image was less than 20 minutes. The ns-TALIF image required over 120 independent images for the reconstruction, all collected at 10 Hz, and resulted in a total collection time of over 3 hours. While an effort was made to ensure consistency between discharge and laser operation parameters, this very long collection time may result in long-term drift and step-to-step fluctuations. Sets of ns-TALIF images were collected at least ten times, to ensure consistency, and they all showed different axial variations within the experimental uncertainty, illustrating the limitation of full planar imaging with a ns-TALIF diagnostic system. Another potential issue involves the relatively large power density coupled to the discharge volume. The discharge power coupled to the discharge under the conditions of this comparison was ~4.5 W. The potential exists for significant gas heating. A simple estimate has been done to determine the upper bound of heating based on the discharge power and the O₂/He mixture flow rate. This estimate suggests that gas heating in the plasma jet volume could exceed 500 K if all coupled energy is thermalized after dissociating the required number of oxygen molecules to produce the signal observed in Figure 10. This is obviously an upper bound, but it illustrates the potential significance of heating. Also, relatively small changes in gas mixture composition or cathode surface oxidation/erosion may well have noticeable impact on the discharge. This has the potential to introduce long-term variability in the TALIF signal over the 3 hour period required for the ns-TALIF image reconstruction. Additionally, the ns-laser-based diagnostic is incapable of simultaneously exciting all three J sublevels of the atomic oxygen transition (see Section 3.5). The relative splitting of atomic oxygen population among these levels was calibrated assuming standard temperature and pressure. If heating is indeed significant, this calibration could be affected, causing under prediction in atomic oxygen number density in heated plasma regions.
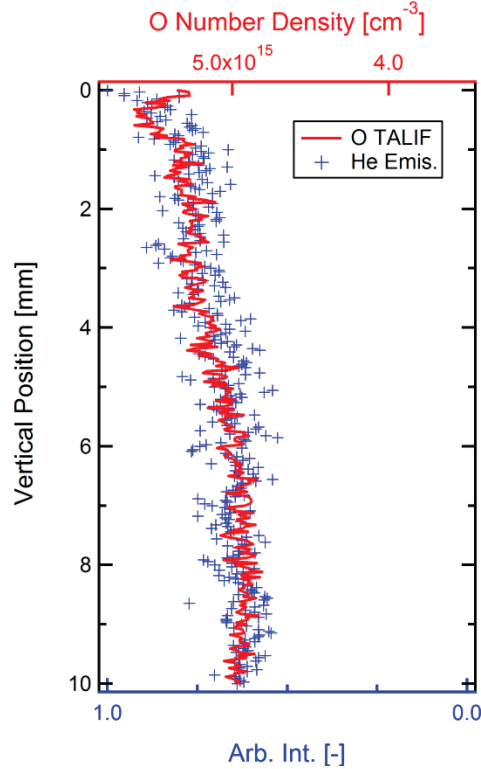
Figure 11: Atomic oxygen number density and volume-averaged emission from the helium (3s ^{3}S → 2p ^{3}P) line collected with an ICCD camera from the centerline of the APPJ operating in a 2% O$_2$/He mixture.

Atomic oxygen distributions were also collected with the CDBDs in an ozone production regime, as shown below in Figure 12. For the ns-TALIF setup, the discharge was operated in a 2% O$_2$ admixture at a pulse repetition rate of 5 kHz, with an average discharge power of 0.56 W; for the fs-TALIF setup, the discharge was operated in a 4% O$_2$ admixture at a pulse repetition rate of 15 kHz, with an average discharge power of 1.0 W.. In this low-power regime, the discharge structure is more annular rather than an axial filament, as shown in Figure 12; a behavior qualitatively illustrated by atomic oxygen distributions determined by both ns-TALIF (Figure 12(left)) and fs-TALIF (Figure 12(right)) diagnostic systems. Additionally, both diagnostic systems show that the annular structure persisted approximately 4 mm downstream from the anode and that the left side of the discharge produced higher atomic oxygen number densities.
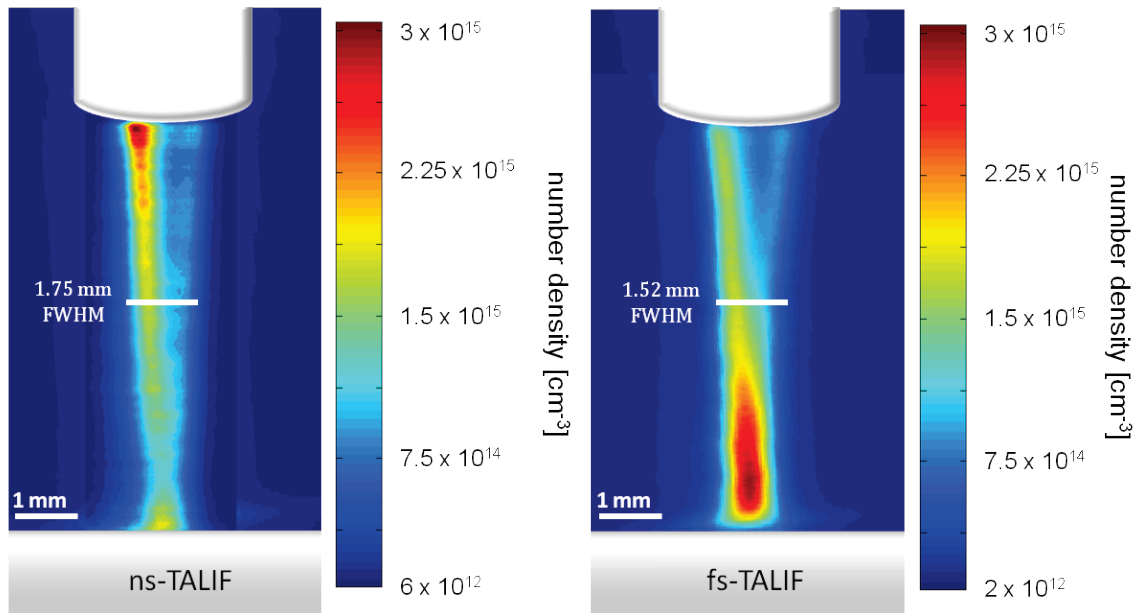
Figure 12: Spatial in-homogeneity comparison between ns-TALIF (left) and fs-TALIF (right) composite images taken in the same APPJ discharge in a 4% O$_2$/He mixture. Significant spatial distribution changes are observed between the two diagnostics; specifically atomic oxygen number density peaks near the anode in the ns-TALIF image and near the cathode in the fs-TALIF image and a 15% difference in FWHM 4 mm down from the anode.

It is interesting to note the differences in peak atomic oxygen TALIF signal and detection limits for both sets of images. While detection limits, discussed below in section 3.5, differ by about a factor of three, the peak atomic oxygen number density for the fs-TALIF composite images is only ~10% higher than the ns-TALIF composite images in both sets of conditions (see Figure 10). This suggests that the differences between the results obtained by the two diagnostics are real since they are larger compared to the experimental uncertainty. The differences in atomic oxygen distribution are likely due to differences in the CDBD sources used in each case, as discussed in section 2.1.

The last item of note between these sets of images is the overall width of the discharge, quantified by the FWHM. The data in Figure 10 show almost no difference between ns and fs diagnostics with this spatial resolution. The data in Figure 12, however, shows a more significant difference. 4 mm down from the anode, where both ns- and fs-TALIF images show relatively small signal levels, the ns-TALIF predicts a discharge filament diameter of 1.75 mm; 15% larger than the 1.52 mm diameter shown in the fs-TALIF images. As discussed in section 3.3, discharge-produced ozone densities are at their highest at these discharge conditions [Sands el al. 2013]. Ozone can be relatively easily dissociated by the large laser fluence, or peak energy intensity, from the ns-laser pulse. This could cause an artificial broadening of the measured filament diameter in the ns-TALIF data and introduce distortion of the spatial distribution of the atomic oxygen number density in the ns-TALIF measurement that are quite difficult to correct for.

3.5. Single shot detection limits

Total signal or efficiency of excitation of the excited state is not the only consideration when determining the value of a given excitation scheme. Another main parameter of interest is the single-shot detection limit. This is the minimum number density of atoms that provides a signal that is distinguishable above the background or read-out noise of the system. There are methods, such as on-chip averaging and electronic multiplication, that are used to reduce the effects of background signal or on-chip noise, but these do not give an accurate measure of single-laser-shot detection limits. For this determination, the on-chip averaging was eliminated and only background subtraction and electronic chip cooling were allowed, if applicable. The single-shot limit in this experiment was defined when the signal-to-noise ratio was 2:1.

For this comparison, both 2% and 4% O$_2$/He mixtures were selected. Multiple spatial locations within the discharge were tested to ensure consistency of the comparison. The single-shot detection limit for the ns-laser based diagnostic was determined to be 6.1×10^{12} cm^{-3}. For the fs-laser-based diagnostic, this limit was determined to be 2.0×10^{12} cm^{-3}. This is a factor of three lower than the ns-laser-based system. The difference is likely indicative of excitation efficiency differences and limitations of the ns-based system largely related to the ns-laser pulse energy variation causing 'noise' levels to be higher (see discussion in section 3.2).

To corroborate this result, the same test was conducted using the PMT-based system instead of the cameras. This comparison was based on point-wise measurements and not two-dimensional images. However, it is another test-bed in which identical measurements can be made with the exception of the incident laser-pulse duration. Under the same conditions as above, the fs-TALIF system demonstrated single-shot detection limit of 3.8×10^{11} cm^{-3}. The ns-TALIF system demonstrated a single-shot detection limit of 6.5×10^{11} cm^{-3}. Each of these limits are approximately an order of magnitude lower than the imaging system was able to obtain and are at most three orders of magnitude lower than established LIF-based detection limits of major radicals [Kohse-Höinghaus 1994, Eckbreth 1998].

3.6. J-sublevel splitting considerations in ns-TALIF calibration

As mentioned above in Section 2.3, for calibration of atomic-oxygen number densities, xenon was selected since the *5p^6 ^{1}S$_0$→6p′[3/2]$_2$* transition in Xe lies very close to the *2p^4 ^{3}P$_{2,1,0}$→3p ^{3}P$_{1,2,0}$* transition in atomic oxygen. When using a ns-laser based diagnostic system, the bandwidth of the ns laser is not sufficient to simultaneously excite all J sublevels. As such, Eqn. 1, given in the generic noble gas calibration discussion in Section 2.3, needs an additional term to compensate for this.

If the atomic oxygen ground state exhibits a thermal population distribution, which is assumed for all cases presented here, the population fraction of a given J-sublevel, where J is the total angular momentum quantum number, can be calculated through Boltzmann statistics. The Boltzmann population fraction is defined in Eqn. 6, where n_J is the population in the J sublevel, E_J is the relative energy above the ground state in cm^{-1}, and T is the local gas temperature.

$$\frac{n_J}{\sum_J n_J} = \frac{(2J+1)\exp\left(\dfrac{-E_J}{k_B T}\right)}{\sum_J (2J+1)\exp\left(\dfrac{-E_J}{k_B T}\right)} = \frac{1}{C_B} \qquad \text{Eqn. 6}$$

The updated calibration equation for ns-TALIF is given below in Eqn. 7 and includes this Boltzmann-distribution correction factor, C$_B$, necessary for calibration of narrow-bandwidth, ns-TALIF diagnostics.

$$n_X = C_B \frac{\eta_{Cal}}{\eta_X} \frac{\Phi^2_{Cal}}{\Phi^2_X} \frac{a_{21_{Cal}}}{a_{21_X}} \frac{\sigma^{(2)}_{Cal}}{\sigma^{(2)}_X} n_{Cal} = C_B \chi \frac{S_X}{S_{Cal}} n_{Cal} \qquad \text{Eqn. 7}$$

The relative sensitivity of this correction factor to temperature is shown in Figure 13. The relative population distribution becomes relatively insensitive to temperature over 1000 K. Thus, for combustion applications, this correction becomes relatively minor, but it can have larger implications at lower temperatures, such as in non-equilibrium plasma applications.
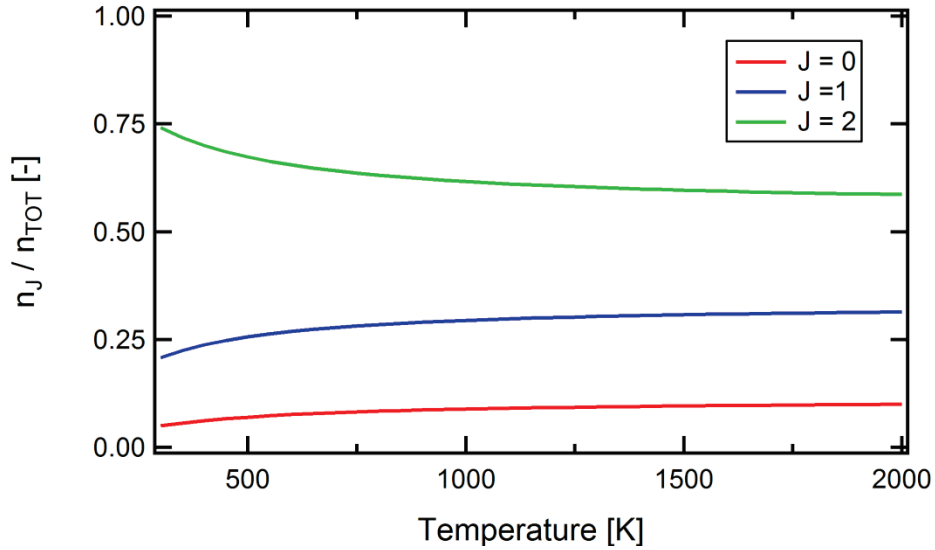
Figure 13: **Relative population of specific J sublevels of atomic oxygen for different temperatures.**

3.7. Off-resonance signal collection

As mentioned previously, one of the significant advantages of the fs-duration laser pulse over ns-duration laser pulses is the inherently large bandwidth of the fs-duration pulse. This increase in bandwidth allows for a larger number of photon pairs capable of the same two-photon excitation. This effect is illustrated in the graphic in Figure 14 and has already been utilized to significant positive effect in non-linear spectroscopy.
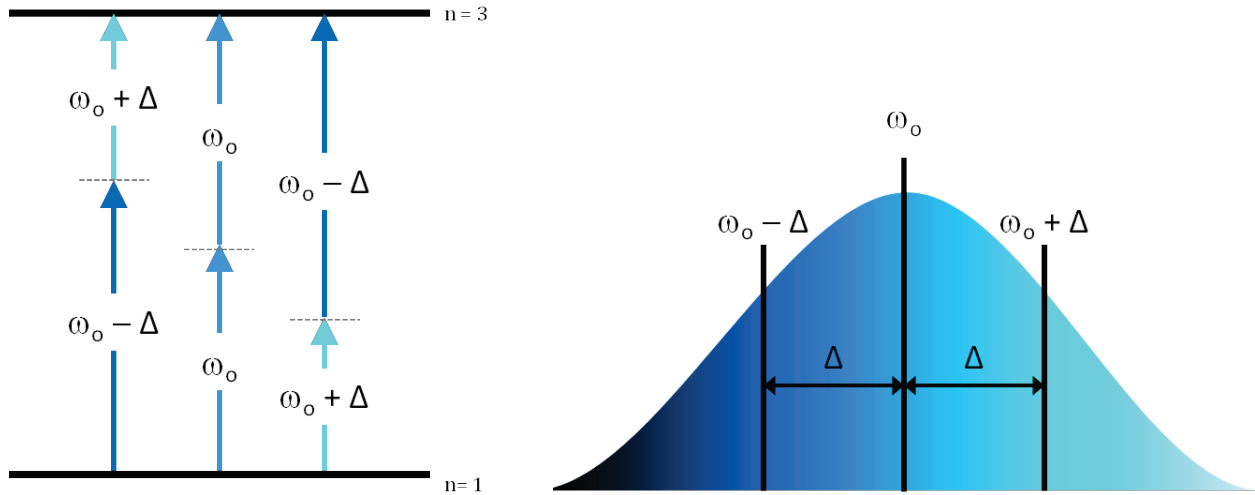
Figure 14: **Graphic showing off-CWL-bandwidth pairing resulting in same energy multi-photon excitation.**

In order to illustrate this point, the center wavelength (CWL) of the incident laser pulse is tuned over an excitation transition and the fluorescence signal is recorded as a function of CWL of the incident radiation. The CWL-dependant fluorescence signal is normalized and compared against the bandwidth of the laser system for both fs- and ns-laser systems. This is shown in Figure 14 for both fs- and ns-based systems for the xenon transition given above in Section 2.3. Xenon was selected for this demonstration as its transition is relatively isolated from other nearby transitions, unlike atomic oxygen, and its relatively strong absorption and fluorescence.
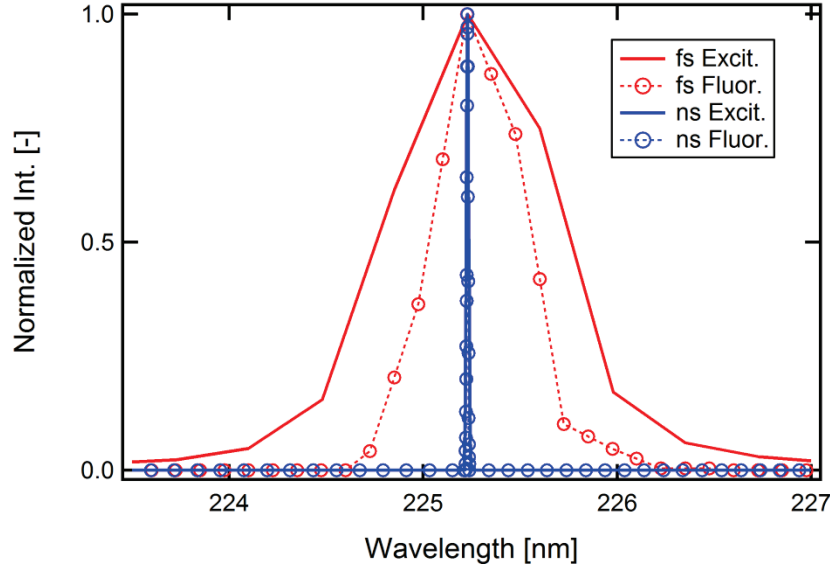
Figure 15: Comparison of fluorescence signals for off-resonant laser excitation wavelength between ns- and fs-laser systems.

A small, but significant, subtlety arises from this comparison: the convolution integral between absorption and incident laser line shapes is no longer accurate. Typically, when deriving the TALIF signal from first principles, a convolution integral of the overlap of the two line shapes is calculated to determine the fraction of the absorption line that is being excited. This convolution ensures that the spectral shape of the laser and absorption lines, as well as any off-resonance mismatch, are accounted for. For ns-laser systems, calibration of TALIF signals assumes are taken in the limit of the monochromatic approximation, in which the absorption line is assumed to have a much larger width than the incident laser pulse bandwidth. For example, a representative atomic oxygen absorption line has line widths of approximately 1.0 cm^{-1} [Niemi et al. 2005] and are dependent on ambient conditions, whereas conventional injection-seeded ns- and ps-laser systems have line widths of ~0.2 cm^{-1}. However, the monochromatic approximation is no longer valid for the fs-based system. The fs-laser bandwidth of over 200 cm^{-1} is significantly larger than the total absorption bandwidth, such that the laser lineshape can be assumed to be constant over a single absorption transition if the laser pulse is centered on the absorption line. However, this also suggests that off-resonance contributions to absorption may be significant enough to invalidate the assumption of using the absorption line width as the new convolution function. More work is required to determine accurately the contribution of off-resonance absorption to the total fluorescence signal and how to take this into account for this new, high-bandwidth fs regime.

3.8. Error analysis

In order to determine the uncertainty of the number densities measured in the present work, an error analysis is performed. This error analysis takes the form of a standard error propagation from calculus. More specifically, if a result $R = R(x, y, z)$ is calculated from a number of parameters with associated uncertainties, then the variation in the result can be expressed in terms of variation of the parameters, as follows in Eqn. 8.

$$dR = \frac{\partial R}{\partial x} dx + \frac{\partial R}{\partial y} dy + \frac{\partial R}{\partial z} dz \qquad \text{Eqn. 8}$$

If the variation of the parameters are small and independent, the differentials can be replaced with finite variations. This is shown in Eqn. 9. This is a generalization of the application of the chain differentiation rule as higher order terms are neglected. Finally, the resultant equation for the variation

22

(absolute error) of the result is divided by the total result, R, to determine the weighting of individual relative errors. This is shown in Eqn. 10.

$$\delta R = \frac{\partial R}{\partial x}\delta x + \frac{\partial R}{\partial y}\delta y + \frac{\partial R}{\partial z}\delta z \qquad \text{Eqn. 9}$$

$$\frac{\delta R}{R} = \frac{x}{R}\frac{\partial R}{\partial x}\frac{\delta x}{x} + \frac{y}{R}\frac{\partial R}{\partial y}\frac{\delta y}{y} + \frac{x}{R}\frac{\partial R}{\partial z}\frac{\delta z}{z} \qquad \text{Eqn. 10}$$

This formulation lends itself to determination of standard deviation. This is determined by summing the squared components of Eqn. 10 and is shown in Eqn. 11 [Kreysizg 1993].

$$\left(\frac{\delta R}{R}\right)^2 = \left(\frac{x}{R}\frac{\partial R}{\partial x}\right)^2\left(\frac{\delta x}{x}\right)^2 + \left(\frac{y}{R}\frac{\partial R}{\partial y}\right)^2\left(\frac{\delta y}{y}\right)^2 + \left(\frac{x}{R}\frac{\partial R}{\partial z}\right)^2\left(\frac{\delta z}{z}\right)^2$$

$$\sigma_R^2 = \left(\frac{x}{R}\frac{\partial R}{\partial x}\right)^2\sigma_x^2 + \left(\frac{y}{R}\frac{\partial R}{\partial y}\right)^2\sigma_y^2 + \left(\frac{x}{R}\frac{\partial R}{\partial z}\right)^2\sigma_z^2 \qquad \text{Eqn. 11}$$

The calibration equation for atomic oxygen number density from section 3.5 is presented again in Eqn. 12 as an example. For error determination purposes, the entire equation can be separated into constants and parameters that affect error generation discussion. Everything else can be lumped together into a single constant that has no associated error.

$$n_O = C_B \frac{\eta_{Xe}}{\eta_O}\frac{a_{Xe}}{a_O}\frac{\sigma_{Xe}^{(2)}}{\sigma_O^{(2)}}\left(\frac{T_{Xe}}{T_O}\frac{E_{Xe}}{E_O}\right)^2\frac{S_O}{S_{Xe}}n_{Xe} = \gamma\left(\frac{T_{Xe}}{T_O}\frac{E_{Xe}}{E_O}\right)^2\frac{\eta_{Xe}}{\eta_O}\frac{a_{Xe}}{a_O}\frac{S_O}{S_{Xe}}n_{Xe} \qquad \text{Eqn. 12}$$

From this simplified equation, we are able to determine eight partial derivatives relating the number density of atomic oxygen to of the parameters. These parameters include atomic oxygen signal level, S_O, xenon signal level, S_{Xe}, incident laser energy for atomic oxygen collection, E_O, incident laser energy for xenon calibration, E_{Xe}, efficiency of atomic oxygen collection system, η_O, efficiency of xenon collection system, η_{Xe}, fluorescence yield of atomic oxygen, $a_O = \dfrac{A_{23,O}}{A_{2,O} + Q_{2,O}}$, and fluorescence yield of xenon,

$a_{Xe} = \dfrac{A_{23,Xe}}{A_{2,Xe} + Q_{2,Xe}}$. This set of partial differential equations is shown below in Eqn. 13.

$$\frac{\partial n_O}{\partial S_O} = \gamma \left(\frac{T_{Xe}}{T_O}\frac{E_{Xe}}{E_O}\right)^2 \frac{\eta_{Xe}}{\eta_O}\frac{a_{Xe}}{a_O}\frac{1}{S_{Xe}}n_{Xe}$$

$$\frac{\partial n_O}{\partial S_{Xe}} = \gamma \left(\frac{T_{Xe}}{T_O}\frac{E_{Xe}}{E_O}\right)^2 \frac{\eta_{Xe}}{\eta_O}\frac{a_{Xe}}{a_O}\frac{S_O}{S_{Xe}^2}n_{Xe}$$

$$\frac{\partial n_O}{\partial E_O} = -2\gamma \frac{T_{Xe}^2}{T_O^2}\frac{E_{Xe}^2}{E_O^3}\frac{\eta_{Xe}}{\eta_O}\frac{a_{Xe}}{a_O}\frac{S_O}{S_{Xe}}n_{Xe}$$

$$\frac{\partial n_O}{\partial E_{Xe}} = 2\gamma \frac{T_{Xe}^2}{T_O^2}\frac{E_{Xe}}{E_O^2}\frac{S_O}{S_{Xe}}\frac{\eta_{Xe}}{\eta_O}\frac{a_{Xe}}{a_O}n_{Xe}$$

$$\frac{\partial n_O}{\partial \eta_O} = -\gamma \left(\frac{T_{Xe}}{T_O}\frac{E_{Xe}}{E_O}\right)^2 \frac{\eta_{Xe}}{\eta_O^2}\frac{a_{Xe}}{a_O}\frac{S_O}{S_{Xe}}n_{Xe}$$

$$\frac{\partial n_O}{\partial \eta_{Xe}} = \gamma \left(\frac{T_{Xe}}{T_O}\frac{E_{Xe}}{E_O}\right)^2 \frac{1}{\eta_O}\frac{a_{Xe}}{a_O}\frac{S_O}{S_{Xe}}n_{Xe}$$

$$\frac{\partial n_O}{\partial a_O} = -\gamma \left(\frac{T_{Xe}}{T_O}\frac{E_{Xe}}{E_O}\right)^2 \frac{\eta_{Xe}}{\eta_O}\frac{a_{Xe}}{a_O^2}\frac{S_O}{S_{Xe}}n_{Xe} = -\gamma \left(\frac{T_{Xe}}{T_O}\frac{E_{Xe}}{E_O}\right)^2 \frac{\eta_{Xe}}{\eta_O}\frac{\frac{A_{23,Xe}}{A_{2,Xe}+Q_{Xe}}}{\left(\frac{A_{23,O}}{A_{2,O}+Q_O}\right)^2}\frac{S_O}{S_{Xe}}n_{Xe}$$

$$\frac{\partial n_O}{\partial a_{Xe}} = \gamma \left(\frac{T_{Xe}}{T_O}\frac{E_{Xe}}{E_O}\right)^2 \frac{\eta_{Xe}}{\eta_O}\frac{1}{a_O}\frac{S_O}{S_{Xe}}n_{Xe} = \gamma \left(\frac{T_{Xe}}{T_O}\frac{E_{Xe}}{E_O}\right)^2 \frac{\eta_{Xe}}{\eta_O}\frac{1}{\frac{A_{23,O}}{A_{2,O}+Q_O}}\frac{S_O}{S_{Xe}}n_{Xe}$$

Eqn. 13

The total estimated error is the sum of the squares of each of these partial derivative. This is given in Eqn. 14.

$$\delta n_O = \sqrt{\sum \left(\frac{\partial n_O}{\partial \phi_i}\right)^2 \delta \phi_i}$$

Eqn. 14

Each individual term for each gas mixture is summarized below in Table 3. Overall, the atomic oxygen fs-TALIF measurements have the smallest overall uncertainties of ±16.9%. The largest uncertainties are associated with atomic oxygen ns-TALIF measurements because the quenching rates were taken from the literature and not measured in-situ. Additionally, the ns-TALIF measurements suffered from increased laser energy fluctuations. The lower fluctuation level in the fs laser system is one of the major factors that leads to lower overall uncertainty compared to that of the ns laser system. Beside the decay rate uncertainties, the next largest uncertainty terms stem from signal fluctuations collected with the high speed imaging system. This is discussed in more depth in section 3.9.

Table 3: Summary of individual uncertainty terms used to determine total uncertainty for atomic oxygen fs-TALIF, and oxygen ns-TALIF, from left to right, respectively.

$(\delta n_O)_{fs}$		$(\delta n_O)_{ns}$	
$\dfrac{\partial n_O}{\partial S_O}$	5.7%	$\dfrac{\partial n_O}{\partial S_O}$	12.5%
$\dfrac{\partial n_O}{\partial S_{Xe}}$	8.4%	$\dfrac{\partial n_O}{\partial S_{Xe}}$	9.1%
$\dfrac{\partial n_O}{\partial E_O}$	2.2%	$\dfrac{\partial n_O}{\partial E_O}$	12.1%
$\dfrac{\partial n_O}{\partial E_{Xe}}$	2.1%	$\dfrac{\partial n_O}{\partial E_{Xe}}$	11.3%
$\dfrac{\partial n_O}{\partial \eta_O}$	1.7%	$\dfrac{\partial n_O}{\partial \eta_O}$	7.7%
$\dfrac{\partial n_O}{\partial \eta_{Xe}}$	1.3%	$\dfrac{\partial n_O}{\partial \eta_{Xe}}$	8.1%
$\dfrac{\partial n_O}{\partial a_O}$	12.4%	$\dfrac{\partial n_O}{\partial a_O}$	18.5%
$\dfrac{\partial n_O}{\partial a_{Xe}}$	3.9%	$\dfrac{\partial n_O}{\partial a_{Xe}}$	11.1%
16.9%		**33.1%**	

4. Conclusion

The performance of fs-TALIF has been compared against ns-TALIF on a number of different metrics. The list below summarizes the main results of this comparison.

- Fs-TALIF signal is up to 15 times stronger than ns-TALIF signal when normalized to incident laser intensity.
- fs-TALIF enabled in-situ measurement of collisional quenching rates over a wider range of pressures and operating conditions than is possible with ns-TALIF.
- The difference in internal architecture of the fs laser system resulted in significantly lower power fluctuations, typically ~2% of full scale, compared to the ns laser system, typically ~11% of full scale, and operation at 1-10 kHz repetition rates instead of the 5-50 Hz with ns laser systems.
- The ability to directly account for quenching and the decreased laser pulse energy fluctuations in the fs-laser system helped reduce the overall experimental uncertainty in atomic oxygen densities from approximately ±30% with ns-TALIF to approximately ±18% with fs-TALIF, depending on experimental conditions.
- Single-shot detection limits of both diagnostics are comparable, on the order of 10^{12} cm^{-3}, with fs-TALIF obtaining lower limits of 2.0×10^{12} cm^{-3} compared to 6.1×10^{12} cm^{-3} with ns-TALIF.
- The lower average power of the fs laser pulse results in significantly lower photo-dissociation, compared to ns-TALIF.
- Two-dimensional images of atomic species distributions can be acquired in minutes with fs-TALIF compared to hours with ns-TALIF.

Combining these factors enables two-dimensional fs-TALIF imaging of much larger regions compared to ns-TALIF with better spatial homogeneity than their ns-TALIF equivalents. The higher laser pulse intensity in the fs diagnostic generates higher fluorescence signal with reduced photolytic interferences while preserving high working pressure quenching rate measurements.

5. References

Aldén M, Edner H, Grafström P and Svanberg S 1982 *Opt Comm* **42**(4) 244

Alekseev V and Setser D W 1996 *J. Phys. Chem.* **100** 5766

Amorim J, Baravian G and Ricard A 1995 *Plasma Chem Plasma Proc* **15**(4) 721

Amorim J, Baravian G, Touzeau M and Jolly J 1994 *J Appl Phys* **76**(3) 1487

Bamford J D, Jusinski L E, and Bischel W K 1986 *Phys. Rev. A* **34**(1) 185-198

Bevington P R and Robinson D K 1992 *Data Reduction and Analysis for the Physical Sciences* 2nd ed. McGraw-Hill, Boston

Bischel W K, Perry B E and Crosley D R 1981 *Chem Phys Lett* **82**(1) 85

Bittner J, Kohse-Hoinghaus K, Meier U and Just Th 1988 *Chem Phys Lett* **143**(6) 571

Bokor J, Freeman R R, White J C and Storz R H 1981 *Phys Rev A* **24**(1) 612

Boogaarts M G H, Mazouffre S, Brinkman G J, van der Heijden H W P, Vankan P, van der Mullen J A M, Schram D C and Döbele H F 2002 *Rev Sci Instrum* **73**(1) 73

Bruce M R, Layne W B, Whitehead C A, and Keto J W 1989 *J. Chem. Phys.* **92** 2917

Clyne M A and Nip W S in *Reactive Intermediates in the Gas Phase*, edited by Setser D W (Academic, New York, 1979)

Czarnetzki U, Miyazaki K, Kajiwara T and Muraoka K 1994 *J Opt Soc Am B* **11**(11) 2155

DiMauro L F, Gottscho R A and Miller T A 1984 *J Appl Phys* **56**(7) 2007

Döbele H F, Mosbach T, Niemi K and Schulz-von der Gathen V 2005 *Plasma Sources Sci Technol* **14** S31

Eckbreth A C 1996 *Laser Diagnostics for Combustion Temperature and Species*. Taylor & Francis, New York.

Frank J H and Settersten T B 2005 *Proc Combust Inst* **30** 1527

Glass-Maujean M, Lauer S, Liebel H, and Schmoranzer H 2000 *J. Phys. B. At. Mol Opt. Phys.* **33** 4593-4601

Goodman J W 1985 *Statistical Optics* Wiley, New York

Hasson V and Nicholls R W 1971 *J. Phys. B: Atom. Molec. Phys.* **4** 1789-1797

Inoue G, Ku J K, and Setser D W 1984 *J. Chem. Phys.* **81** 5760-5774

Kohse-Höinghaus K 1994 *Prog. Energy Combust. Sci.* **20** 203-279

Kreyszig E 1993 *Advanced Engineering Mathematics* 7th ed. John Wiley and Sons, New York

Kulatilaka W D, Lucht R P, Roy S, Gord J R and Settersten T B 2007 *Appl Opt* **46**(19) 3921

Kulatilaka W D, Patterson B D, Frank J H and Settersten T B 2008 *Appl Opt* **47**(26) 4672

Kulatilaka W D, Frank J H, Patterson B D and Settersten T B 2009 *Appl Phys B* **97** 227

Kulatilaka W D, Gord J R, Katta V R and Roy S 2013 *Opt Lett* **37**(15) 3051

Kulatilaka W D, Gord J R and Roy S 2014 *Appl Phys B-Rapid Communications*, **116**(1) 7

Meier U, Kohse-Hoinghaus K, Schafer L and Klages C-P 1990 *Appl Opt* **29**(33) 4993

Miyazaki K, Kajiwara T, Uchino K, Muraoka K, Okada T and Maeda M 1996 *J Vac Sci Technol A* **14**(1) 125

Molina L T and Molina M J 1986 *J. Geophys. Res: Atmos.* **91** 14501-14508

Niemi K, Schulz-von der Gathen V and Döbele H F 2001 *J Phys D: Appl Phys* **34** 2330

Niemi K, Schulz-von der Gathen V, and Döbele H F 2005 *Plasma Sources Sci. Technol.* **14** 375

Ono R, Takezawa K, and Oda T 2009 *J. Appl. Phys.* **106** 043302

Ono R 2016 *J. Phys. D: Appl. Phys.* **49** 083001

Preppernau B L, Dolson D A, Gottscho R A and Miller T A 1989 Plasma Chem Plasma Process **9**(2) 157

Preppernau B L, Pearce K, Tserepi A, Wurzberg E and Miller T A 1995 Chem Phys **196** 371

Samukawa S, Hori M, Rauf S, Tachibana K, Bruggeman P, Kroesen G, Whitehead J C, Murphy A B, Gutsol A F, Starikovskaia S, Kortshagen U, Boeuf J-P, Sommerer T J, Kushner M J, Czarnetzki U, and Mason N 2012 *J. Phys. D: Appl. Phys.* **45** 253001

Sands B L and Ganguly B N 2013 *J Appl Phys* **114** 243301

Saxon R P and Eichler J 1986 *Phys Rev A* **34**(1) 199

Schmidt J, Sands B, Kulatilaka W, Roy S, Scofield J, and Gord J 2015 *Plasma Sources Science and Technology* 032004

Settersten T B, Dreizler A and Farrow R L 2002 *J Chem Phys* **117**(7) 3173

Tserepi A D, Dunlop J R, Preppernau B L and Miller T A 1992 *J Appl Phys* **72**(7) 2638

van Gessel A F H, van Grootel S C, and Bruggeman P J 2013 *Plasma Sources Sci. Technol.* **22** 055010

Welge K H and Atkinson R 1976 *J. Chem. Phys.* **64** 531-538

Zhang S, van Gessel A F H, van Grootel S C, and Bruggeman P J 2014 *Plasma Sources Sci. Technol.* **23** 025012

Zikratov G and Setser D W 1996 *J. Chem. Phys.* **104** 2243